

April 29, 2014

Submitted to J. Mech. Phys. Solids

Computing elastic moduli on 3-D X-ray computed tomography image stacks

E.J. Garboczi  
Material and Structural Systems Division  
National Institute of Standards and Technology  
Gaithersburg, MD 20899 USA

V.I. Kushch  
Institute for Superhard Materials  
National Academy of Science of Ukraine  
2 Avtozavodskaya Street  
04074 Kyiv Ukraine

#### Abstract

A numerical task of current interest is to compute the effective elastic properties of a random composite material by operating on a 3D digital image of its microstructure obtained via X-ray computed tomography (CT). The 3-D image is usually sub-sampled since an X-ray CT image is typically of order  $1000^3$  voxels or larger, which is considered to be a very large finite element problem. Two main questions for the validity of any such study are then: can the sub-sample size be made sufficiently large to capture enough of the important details of the random microstructure so that the computed moduli can be thought of as accurate, and what boundary conditions should be chosen for these sub-samples? This paper contributes to the answer of both questions by studying a simulated X-ray CT cylindrical microstructure with three phases, cut from a random model system with known elastic properties. A new hybrid numerical method is introduced, which makes use of finite element solutions coupled with exact solutions for elastic moduli of square arrays of parallel cylindrical fibers. The new method allows, in principle, all of the microstructural data to be used when the X-ray CT image is in the form of a cylinder, which is often the case. The appendix describes a similar algorithm for spherical sub-samples, which may be of use when examining the mechanical properties of particles. Cubic sub-samples are also taken from this simulated X-ray CT structure to investigate the effect of two different kinds of boundary conditions: forced periodic and fixed displacements. It is found that using forced periodic displacements on the non-geometrically periodic cubic sub-samples always gave more accurate results than using fixed displacements, although with about the same precision. The larger the cubic sub-sample, the more accurate and precise was the elastic computation, and using the complete cylindrical sample with the new method gave still more accurate and precise results. Fortran 90 programs for the analytical solutions are made available on-line, along with the parallel finite element codes used.

Keywords: composite; analytical solutions; boundary conditions; X-ray computed tomography; elastic moduli

## 1. Introduction

Theoretical study of the linear elastic properties of real materials, based on their microstructure, is an important branch of materials science and physics. Various pure mathematical efforts include exact bounds, exact dilute limits, exact solutions of simple periodic composites, approximate effective medium theories based on those exact dilute limits, and many more empirical formulae whose basis is a plausible mathematical form with constants fit to experimental results (Milton, 2002; Mura, 1982; Torquato, 2002). Obtaining 2-D images of microstructure using various forms of microscopy, along with knowledge of the elastic moduli of various phases, allows the application of finite element and other computational techniques to directly compute the 2-D elastic moduli of random materials (Langer et al., 2001). With the advent of experimental techniques like X-ray computed tomography (CT) (Kak and Slaney, 2001), along with image analysis techniques (Russ, 2007), 3-D images of microstructure can be obtained and 3-D computations can be made directly on real microstructures to compute the effective elastic properties of the material (Wismans et al., 2010; Faessel et al., 2005; Tsuda et al., 2008; Geandier et al., 2003; Scocchi et al., 2012).

X-ray CT image sets are typically of order  $1000^3$  voxels or larger, which are considered to be very large finite element problems if every voxel is taken to be a finite element (Garboczi and Day, 1995; Garboczi, 1998; Bohn and Garboczi, 2003). Adaptive meshing can be used to reduce the computational size but that usually loses some material resolution, the finite element problem remaining is still a large computational problem, and solving the random shape and size mesh usually requires a sophisticated commercial program. Although the size of the problem really requires parallel processing, licenses for parallel operation on more than a few processors for commercial codes can be quite expensive. A public domain parallel finite element code is available that is specialized for 3-D digital images. The code is written in Fortran 90, where each voxel is a tri-linear finite element (Bohn and Garboczi, 2003) and is used herein.

X-ray CT experiments are usually performed on cylindrical shapes, whether molded or cored from a larger piece, so that the sample presents a uniform aspect to the X-ray beam as the sample rotates. Recently, an X-ray tomography technique has been developed called interior tomography (Yu et al., 2009), where the region of interest is only in the interior of the sample. In this case, the image becomes exactly cylindrical, regardless of the overall sample shape, because the Fourier transform mathematics used drills a "virtual core" through the sample interior. Therefore, the result of an X-ray study is often a stack of circular images that make up a 3D cylindrical microstructure. The usual method used to study the elastic moduli of such a large cylindrical sample is not to use the entire cylinder of data, but to cut out a smaller piece of microstructure to work on, usually a cube. If such a piece is taken, some of the microstructure is not used and therefore lost to the elastic moduli computation, making the accuracy of the computation hard to judge since often the elastic moduli of the material studied is not known very well. One chooses a cubic shape for numerical ease in the application of boundary conditions. Periodic boundary conditions are usually thought of as the best boundary conditions to use examining a small sample of larger microstructure, in order to reduce the effect of the (sometimes) large surface area to volume ratio encountered in a small sample. Since the sample has been cut out physically or virtually or molded in some way, it is not periodic, and so periodic boundary conditions cannot, in principle, be directly applied. The usual solution is to apply fixed load or fixed

displacement conditions on the piece of random microstructure (i.e. all sides have fixed displacements or fixed stresses or some combination). The effect of the choice of boundary conditions on the accuracy of the computation is also hard to judge, for the same reason as when choosing sub-sample size.

This paper introduces a new technique that both enables the total microstructure to be used for cylindrical images, and gets around the problem of applying boundary conditions to the edge of the sample. It shows how the entire cylinder-shaped X-ray CT data can be embedded into a uniform medium in a rectangular unit cell and the whole system solved with a finite element solver using periodic boundary conditions for the composite unit cell. The effective properties of the real material can then be accurately extracted using an analytical solution for the elastic moduli of square arrays of parallel cylindrical fibers. The accuracy of this technique is dependent on having highly accurate numerical solutions of these geometrical arrangements, which are available (Kushch, 2013). This method can also be used with spherical pieces of microstructure and exact solutions for cubic arrays of spheres (see Appendix). This alternative approach could be useful for spherical particles, where the elastic properties of the whole particle need to be analyzed, not just a rectangular prism-shaped piece. For both these new methods, which avoid applying boundary conditions to the actual sample, we have made both the analytical solutions and the parallel finite element Fortran 90 programs available on-line (Garboczi and Kushch, 2014).

To evaluate the accuracy and uncertainties of our new method and various shape and size sub-samples and choices of boundary conditions, a large three-phase random composite system with geometric periodic boundary conditions is used whose elastic moduli are very accurately known numerically for two different sets of phase moduli. This is the “material” data. A cylinder is taken out of this system, which then becomes the “X-ray CT” data. The elastic moduli of different size cubic sub-samples of this cylindrical microstructure are computed, using the new method for the entire cylindrical piece and forced periodic vs. fixed displacement boundary conditions for the cubic sub-samples. The results are quantitatively compared to show the differences between the boundary conditions sub-sample sizes used and to display the advantages of the new method.

## 2. Computational finite element procedures

We use a digital-image-based finite element method (FEM) to solve for the elastic properties of random microstructures (Garboczi and Day, 1995; Garboczi, 1998; Bohn and Garboczi, 2003). This technique was designed to operate on periodic random microstructures, although it can be successfully used to study simple shapes like the dilute limit of rectangular blocks (Garboczi et al., 2006; Garboczi and Douglas, 2012) embedded in a periodic unit cell. If the random microstructure comes from a model, then digital resolution scaling (Roberts and Garboczi, 2000; 2002) can be successfully used to obtain more accurate solutions for effective elastic properties. The code uses Message Passing Interface (MPI) parallelization (Bohn and Garboczi, 2003) to enable computations on large systems. Currently, the largest size we have tried has been approximately  $1000^3$  voxels, where each cubic voxel is a tri-linear finite element. The system is broken up into a number of layer stacks oriented normal to the z direction, where the number of

processors used is typically  $nz/4$  to  $nz/2$ , where  $nz$  = the total number of layers in the  $z$  direction. Each processor controls one stack that is several voxels thick and communicates with the processor below and above it. Details of the parallelization process can be found in the manual for the parallel program (Bohn and Garboczi, 2003). The manual for the scalar version of the code gives more theoretical and computational details (Garboczi, 1997) of the finite element portion of the computation. Both the scalar and parallel versions are freely available on-line (Garboczi, 1997). A strain is applied and the average stress, averaged over each voxel and then the entire system, is computed. The average strain is just equal to the applied strain, because of the periodic displacement boundary conditions, so the effective moduli are taken from the components of the average stress tensor. For example, if all the applied strains were zero except for  $\varepsilon_1$ , then all six components of the elastic moduli tensor with the first index equal to one could be determined, since

$$\langle \sigma_i \rangle = C_{ij} \langle \varepsilon_j \rangle \quad (1)$$

By processing a cylindrical stack of X-ray CT images, a rectangular prism-shaped piece can be clipped out and either periodic boundary conditions or fixed displacement boundary conditions are imposed. Although the piece is not really periodic, one can still use periodic boundary conditions, thinking of the cubic piece as the unit cell in a larger periodic structure. In this paper, it was easier to apply fixed displacement boundary conditions using the scalar versions of this finite element code, while the parallel code was used for the forced periodic computations. The parallel and scalar versions have been shown to give identical results for identical microstructures (Bohn and Garboczi, 2003).

The new method introduced in this paper allows the entire cylindrical microstructure to be embedded in a rectangular parallelepiped cell of uniform material. Details of the analytical solution part of this new technique will be discussed in the next section. The cylindrical microstructure is embedded in a box of uniform material that has two equal edges,  $L$ , and a third edge that is equal in length to the height of the cylinder. This method analyzes the entire scanned microstructure without wasting any geometrical detail. The two equal edges of the box should be at least 40 voxels larger than the diameter of the cylinder's circular cross-section to give sufficient resolution for an accurate solution of the elastic displacement fields between the cylinder and its periodic reflections. Figure 1 shows a schematic view of this composite unit cell.

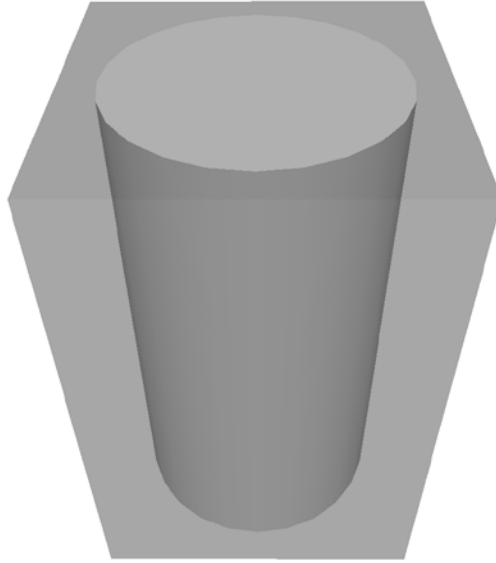


Figure 1: Schematic view of a cylinder centered on and oriented normal to the square face of a rectangular prism-shaped box.

For the cylinder-box system, using periodic boundary conditions means that the top and bottom of the cylinder will match periodically. This can just be forced, or some kind of boundary matching could be done. For example, in the case of a cellular microstructure, it is easy to cover the bottom of the cylinder with a thin artificial cell wall that will satisfy periodic boundary conditions with only a very small change in the overall elastic moduli. Alternately, a very thin layer of the uniform embedding material can be added to the bottom of the cylinder, with similar results. The simplest method is just to force the periodic boundary conditions, which is probably the most accurate method, as will be demonstrated below on the cubic sub-samples.

We focus on the case where the real microstructure (on average) is expected, and the uniform embedding medium is known, to be elastically isotropic. For this case, the computed elastic moduli tensors are isotropically or spherically averaged, which means that the elastic tensor is integrated over the spherical polar angles and normalized by  $4\pi$  (Watt and Peselnick, 1980; Watt, 1980). Since these two phases are each isotropic, there are really only four independent quantities, the exactly known bulk and shear moduli for the embedding medium and the effective composite bulk and shear moduli for the microstructure cylinder. The two independent moduli of the embedding medium are chosen before the computation, so that there are only two unknowns left in the problem, the effective composite bulk and shear moduli of the real microstructure. The cylinder-box system has tetragonal symmetry, so has six independent moduli. Since these six moduli come from only two unknowns, we choose to spherically average the numerical moduli of each system so as to end up with a bulk ( $K$ ) and a shear modulus ( $G$ ) for each composite system (Watt and Peselnick, 1980; Watt, 1980), effectively averaging over the entire system and individual elastic moduli tensor elements. The equations are given below, for a general crystal symmetry (Meille and Garboczi, 2001) – the tetragonal case is obviously a bit simpler. The notation “(a)” was introduced in eq. (2) to simplify the form of eq. (3) and was chosen since eq. (2) denotes simple numerical averages (“a” for average). Although  $C_{ij} = C_{ji}$  in principle, numerically, due to small errors in the solution process, there can be small differences

between  $C_{ij}$  and  $C_{ji}$ , so they are all averaged together. It should also be noted that numerically, tensor elements such as  $C_{14}$  and  $C_{56}$  can be non-zero but are much smaller than the main tensor elements. These elements do not come into the spherical averaging procedure.

$$\begin{aligned} c11(a) &= \frac{1}{3}(C_{11} + C_{22} + C_{33}) \\ c12(a) &= \frac{1}{6}(C_{12} + C_{13} + C_{23} + C_{21} + C_{31} + C_{32}) \\ c44(a) &= \frac{1}{3}(C_{44} + C_{55} + C_{66}) \end{aligned} \quad (2)$$

$$\begin{aligned} G &= \frac{1}{5} [c11(a) - c12(a) + 3 c44(a)] \\ K &= \frac{3}{5} c11(a) + \frac{2}{5} c12(a) + \frac{4}{5} c44(a) - \frac{4}{3} G \end{aligned} \quad (3)$$

The focus of this paper is on large-scale finite element computations, so we try to use as few choices of strain as possible in order to minimize computational effort. Since all the  $C_{ij}$ ,  $i, j = 1, 2, 3$  entries are required to be known independently, as can be seen from eq. (2), we need to do at least three runs with  $\varepsilon_1$ ,  $\varepsilon_2$ , and  $\varepsilon_3$ , each separately non-zero and the other strains zero. For shear, since all we need is the average of  $C_{44}$ ,  $C_{55}$ , and  $C_{66}$ , for the fourth run we can apply all three shear strains simultaneously. Applying the shear strains separately would allow separate determination of moduli like  $C_{14}$  and  $C_{56}$ , which do contribute to the average stress in this case, since all the shear strains are applied simultaneously, but we have found that these terms are small and have alternating signs, so they tend to cancel with each other. We have checked a typical system used in this paper, computing the sum of the shear moduli both ways, and the end result only differs by 0.1 % or less between the two methods of applying the strains.

### 3. Simple geometry composite solutions

If we want to use the entire cylindrical microstructure from X-ray CT images, we need the embedding box to be as small as possible, in order to minimize the size of the system to be computed. For the cylinder-box case, the volume fraction will be, for a cylinder of diameter  $D$  and box edge length  $L$ ,  $(D/L)^2$  times the maximum value of  $\pi/4 = 0.7854$ . As was stated earlier, the minimum value of  $L$  is approximately  $D + 40$ .  $D$  is usually a minimum of 200, so the volume fraction of the cylinder inside the embedding box will be at least  $\pi/4(200/240)^2 = 0.54542$ . If  $D = 1000$ , then this volume fraction = 0.7261. Accurately solving this composite problem analytically, assuming isotropic and uniform elastic moduli in both phases, is much harder as the volume fraction approaches the maximum value. Exact solutions for these cases, which are accurate even for volume fractions near  $\pi/4$ , have been worked out (Kushch, 2013).

The geometry shown in Fig. 1 is a unit cell of a periodic composite made up of a square array of aligned circular fibers embedded in a matrix. In line with this, the problem we consider can be viewed as the following "inverse" homogenization problem: given the properties of the matrix and the effective properties of the composite, find the properties of the fiber. The

micromechanics of fibrous composites are now well developed, so we can use the available solutions of the homogenization problem. However, not all of them are equally appropriate for our purpose: our choice is motivated by the following reasons. First, the problem we consider is, like any inverse problem, ill-conditioned. Therefore, a high solution accuracy is critically important, making it impossible to use approximate methods. Second, the inverse procedure described in the next section implies the homogenization problem has to be solved repeatedly. Therefore, the numerical efficiency of the method is also important. The multipole expansion method used herein meets the above requirements for accuracy and computational effort.

Lord Rayleigh (Rayleigh, 1892) was the first to study the conductivity problem for a periodic fiber composite. In the elasticity theory context, this problem is mathematically equivalent to the out-of-plane (e.g., xz, yz) shear problem. The complete solution to this problem has been obtained by Perrins et al. (Perrins et al., 1979). Pobedrya (Pobedrya, 1984) was probably the first to obtain a complete solution for the effective elastic stiffness tensor (all six independent moduli) for a composite with a square array of fibers. His solution, as well as a series of more recent works (Rodriguez-Ramos et al., 2001 and references therein), are based on using the doubly periodic Weierstrass elliptic functions. Alternatively, a Rayleigh-type multipole expansion approach has been applied (Kushch, 2008) to study the multiple fiber unit cell model of a fibrous composite. A detailed account of the method is given elsewhere (Kushch, 2013); here, we provide only the necessary formulas.

The effective stiffness tensor of a periodic composite with a square array of circular inclusions and infinitely extended in the out-of-plane direction involves six components. They are  $C_{11}(=C_{22})$ ,  $C_{33}$ ,  $C_{12}$ ,  $C_{13}(=C_{23})$ ,  $C_{44}(=C_{55})$  and  $C_{66}$ . They are all calculated from Eq. (1) by solving a series of unit cell problems and averaging the obtained local stress field, so that  $C_{ij} = \langle \sigma_i \rangle$ , where  $\sigma_i$  corresponds to the uniaxial applied strain  $\langle \varepsilon_j \rangle = 1$ . The general homogenization problem can be split into three independent sub-problems of 2D elasticity theory. They are (1) out-of-plane shear, (2) plane strain and (3) generalized plane strain. These problems can be solved separately to get the complete set of the effective elastic moduli of the periodic composite.

**Out-of-plane shear**  $\langle \varepsilon_i \rangle = \delta_{i4}$ . The multipole strengths  $A_k$  are found from the system of linear algebraic equations

$$\frac{(\tilde{G}+1)}{(\tilde{G}-1)} A_k + \sum_{n=1}^{n_{\max}} A_n \eta_{nk} = -\delta_{k1} \quad (k = 1, 2, \dots, n_{\max}); \quad (4)$$

where  $\delta_{k1}$  is the Kronecker's delta and  $\tilde{G} = G_1/G_0$ . The total number of equations (and unknowns  $A_n$ )  $n_{\max}$  is taken sufficiently large to get a fully convergent solution. For example,  $n_{\max} = 16$  provides 5-digit accuracy of solutions for the fiber volume fraction  $c \leq 0.7$  for a whole  $\tilde{G}$  range (Perrins et al., 1979); for  $c = 0.77 = 0.98c_{\max}$ ,  $n_{\max} = 40$ . The matrix coefficients  $\eta_{nk}$  in eq. (4) are given by the formula

$$\eta_{nk} = (-1)^k \binom{n+k-1}{k} \frac{S_{n+k}}{a^{n+k}},$$

where  $S_n$  are the standard harmonic lattice sums (Berman & Greengard, 1994),  $a = \frac{2L}{D} = \sqrt{\pi/c}$ , and  $c$  is the fiber volume fraction. The formula for the effective stiffness tensor element  $C_{44}$  involves only the first dipole moment  $A_1$  found from Eq. (4):

$$C_{44} = G_0(1 - 2cA_1). \quad (5)$$

**In-plane strain.** In the plane strain formulation, we consider two problems:  $\langle \varepsilon_i \rangle = \delta_{i1}$  (in-plane strain) and  $\langle \varepsilon_i \rangle = \delta_{i6}$  (in-plane shear). A solution to both these problems is given by a simultaneous solution of the following linear system

$$\begin{aligned} \Omega_1 B_k - \delta_{k1} 2c \operatorname{Re} \left( A_k - \frac{B_k}{\kappa_0 - 1} \right) - \sum_{n=1}^{n_{\max}} (A_n + \delta_{k1} \overline{A_n}) \eta_{nk} &= C_k; \\ \Omega_2 A_k - \delta_{k1} [c(A_k \kappa_0 + \overline{A_k}) + B_k] + \sum_{n=1}^{n_{\max}} (\overline{A_n} \zeta_{nk} - B_n \eta_{nk}) &= D_k; \end{aligned} \quad (6)$$

$$k = 1, 2, \dots, n_{\max}.$$

Here,  $A_k$  and  $B_k$  are multipole strengths (complex, in general), where the overline  $\overline{A_k}$  denotes the complex conjugate of  $A_k$ . Also,

$$\Omega_1 = \frac{(2\tilde{G} + \kappa_1 - 1)}{\tilde{G}(\kappa_0 - 1) - (\kappa_1 - 1)} \delta_{k1} + (1 - \delta_{k1}) \frac{(\tilde{G} + \kappa_1)}{(\tilde{G}\kappa_0 - \kappa_1)}$$

and

$$\Omega_2 = \frac{(\tilde{G}\kappa_0 + 1)}{(\tilde{G} - 1)},$$

where  $\kappa_i = 3 - 4\nu_i$  ( $i = 0, 1$ ) and  $\nu_i$  is the Poisson ratio of the  $i$ -th material phase. In what follows, we will also use, where convenient, the Lamé modulus  $\lambda$  and the bulk modulus  $K$ , which are related to the other isotropic elastic constants by

$$\lambda = \frac{2G\nu}{1 - 2\nu} = \frac{3K\nu}{1 + \nu}; \quad K = \frac{2G(1 + \nu)}{3(1 - 2\nu)}.$$

The matrix coefficients of Eq. (6) involve the already mentioned harmonic sums  $\eta_{nk}$  and the bi-harmonic sums  $\zeta_{nk}$  defined as

$$\zeta_{nk} = (-1)^k \frac{(n+k)!}{k!(n-1)!} \left[ \frac{T_{n+k+2}}{a^{n+k}} - (n+k+1) \frac{S_{n+k+2}}{a^{n+k+2}} \left( \frac{1}{n+1} + \frac{1}{k+1} \right) \right],$$

where  $T_n$  are the standard biharmonic 2P lattice sums (Movchan et al., 1997). The only non-zero elements of the right-hand vector of Eq. (6) are

$$C_1 = -\frac{1}{2}(1 + \sqrt{-1}); \quad D_1 = \frac{1}{2(1 - 2\nu_0)}.$$

The effective stiffness tensor elements  $C_{11}$  and  $C_{12}$  are readily found from the equations

$$\begin{aligned} C_{11} + C_{12} &= \frac{2G_0}{(1 - 2\nu_0)} [1 + 4c(1 - \nu_0)B_1]; \\ C_{11} - C_{12} &= -2G_0 [1 - 8c(1 - \nu_0)\text{Re}A_1]; \end{aligned} \quad (7)$$

whereas

$$C_{66} = G_0 [1 - 8c(1 - \nu_0)\text{Im}A_1]$$

Only the dipole moments  $A_1$  and  $B_1$  enter the expressions for the in-plane effective elastic moduli.

**Generalized plane strain:**  $\langle \varepsilon_i \rangle = \delta_{i3}$ . The solution to the generalized plane strain problem is also given by eq. (6), with the only non-zero right-side vector element being

$$C_1 = \frac{(\kappa_1 - 1)(\lambda_1 - \lambda_0)}{2[G_1(\kappa_0 - 1) - G_0(\kappa_1 - 1)]}.$$

Evaluation of the effective stiffness tensor elements,  $C_{13}$  and  $C_{33}$ , uses the formulas

$$\begin{aligned} C_{13} &= \lambda_0 + 2c(\lambda_0 + 2G_0)B_1; \\ C_{33} &= \lambda_0 + 2G_0 + c \frac{3(G_1 - G_0)(K_1 - K_0) + 2(\lambda_1 - \lambda_0)(\lambda_0 + 2G_0)B_1}{(\lambda_1 + G_1) - (\lambda_0 + G_0)}; \end{aligned} \quad (8)$$

and completes the solution.

Numerical implementation of the described procedure is straightforward. An accurate linear solver for eqs. (4) and (6) is the only standard subroutine required. The Fortran 90 source code for the evaluation of  $C_{ij}$  is provided in (Kushch, 2013) and on-line (Garboczi and Kushch, 2014). A final note - the two phases actually do not have to be isotropic - analytical solutions (Kushch, 2013) can also be given for anisotropic materials. The programs contained in (Garboczi and Kushch, 2014) are only for elastically isotropic materials.

#### 4. Test cases for new method

Combining finite element computations and the above analytical results, we can compute the effective moduli of a cylindrical microstructure sample. We first directly compute the overall elastic moduli of the cylinder microstructure embedded in a box. Then, knowing the elastic moduli of the embedding medium, we use the analytical results of Section 3 to inversely find the isotropic bulk and shear moduli for the inclusion that best reproduces the numerical results for the entire system. In the real case where the inclusion is actually a piece of random

microstructure, with more than one phase, this procedure assigns effective composite moduli to the microstructure. We first test this method using uniform inclusions.

A cylindrical test case, represented by voxels, is embedded in a cubic unit cell having  $D = 360$  and  $L = 400$ , with  $E_0 = 10$  GPa and  $\nu_0 = 0.25$  (matrix), and  $E_1 = 1$  GPa and  $\nu_1 = 0.1$  (inclusion). The digital volume fraction of the cylinder in this simple composite is 0.636125, and the composite elastic moduli computed via FEM were  $K = 1.632570$  GPa and  $G = 1.244749$  GPa. Table 1 gives the results for the cylinder moduli for this test case. Remember that the cylinder+box case is anisotropic, so the composite values of  $K$  and  $G$  come from the spherically averaged elastic moduli tensor for the entire system.

Table 1: The inverse problem for a cylinder (1) - box (0) test case. The table lists the computed and theoretical composite moduli, and the actual and computed values of the individual phase moduli and their percent difference.

System (size in voxels)		Matrix (0)	Inclusion (1)	FEM composite	Theory composite	Diff (%)		Predicted inclusion modulus (1)	Diff (%)
Cylinder diameter (360) in cube (400)	Bulk modulus (GPa)	20/3	5/12	1.632570	1.633825	-0.1		0.415200	-0.35
	Shear modulus (GPa)	4	5/11	1.244749	1.245218	-0.04		0.454741	0.04

One should note that the column marked “Theory composite” is the prediction from Section 3 for the moduli of the entire composite system based on the exact value of the volume fraction, based on the values of  $D$  and  $L$ , which differs by about 0.07 % from the digital volume fraction. This method is then used, as described below, along with the FEM composite result, to give the data in the column marked “Predicted inclusion modulus (1)”. The result for the inclusion bulk modulus can be expressed as 4.9824/12 GPa and the shear modulus as 5.0022/11 GPa, in order to more easily compare to the given moduli. It is interesting that the errors on the inverse process are similar to the errors on the forward process. The main source of difference between theory and FEM is the fact of the voxel approximation of the curved surface of the cylinder.

Representing the cylinder by a higher density of voxels will cause the error to decrease, and digital resolution scaling can make the difference very small (Roberts and Garboczi, 2000, 2002; Garboczi et al. 2006; Garboczi and Douglas, 2012). The analytical theory is exact, but there could be some very small error in the approximations used in computing the various series involved (see Section 3). This error is much smaller than the finite resolution error in the FEM results.

The program that implements this “backwards” procedure is simple. A reasonable guess can be made for the cylinder moduli. Starting values for both K and G are chosen well under this value and the theoretical moduli are computed. Some manual adjustment may be necessary in order to get the starting values below the actual values. An increment is chosen so that 10 steps in this increment in K and G will take the theoretical prediction to well above what was computed by FEM for the composite. The values of K and G in this first iteration are chosen to separately minimize the deviations from the known composite K and G and then the increment is refined and a new starting point is chosen so that the search grid encompasses these new values. This procedure is run a number of times (about 10 is usually enough), giving an answer for the bulk and shear moduli of the cylindrical inclusion that is unchanging to 6 digits or more.

## 5. Effect of different boundary conditions on a realistic random microstructure

A sample random microstructure was prepared – this is the “material” from which we will take a cylindrical piece via simulated X-ray CT. When using a real material sample, the exact moduli of that particular sample are rarely known, but only the moduli of the much larger material piece from which the sample is taken. The moduli of the constituent phases are also often known. Therefore, using a model material whose moduli are exactly known is a good choice. The original random microstructure is periodic with a cubic unit cell 800 voxels on a side. Freely overlapping digital spheres of diameter 41 voxels were inserted at random centers, using periodic boundary conditions. In this case, periodic boundary conditions means that if any part of a sphere lay outside the unit cell, it would be brought back in on the opposite side of the cell. This results in a two-phase structure, consisting of the matrix (phase 0) and the volume inside the overlapping spherical inclusions (phase 1). However, we wanted our test case “material” to be more complicated, so when each sphere was inserted into the matrix, the sphere was chosen to be phase 1 with a probability of 0.3 and phase 2 with a probability of 0.7. The final volume fractions were:  $c_0 = 0.35006257$ ,  $c_1 = 0.19615083$ , and  $c_2 = 0.45378659$ , as determined in the  $800^3$  digital image. Figure 2 shows one of the possible 800 x 800 voxel cross-sections of the complete 3-D periodic structure. More than one circle size is seen because the slice cuts through the monosize spheres at random heights with respect to their centers.

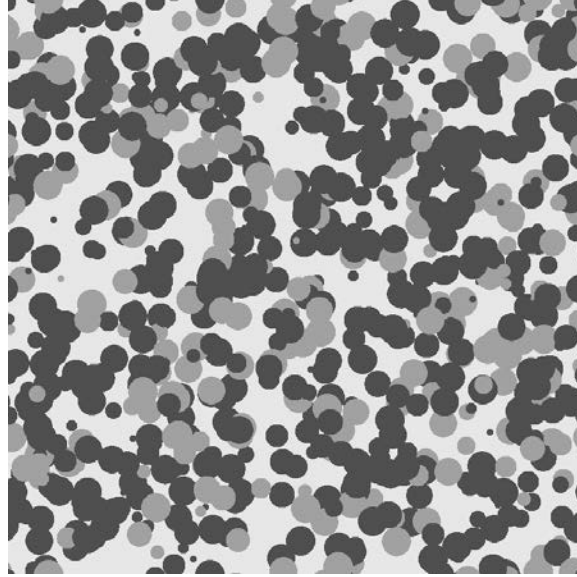


Figure 2: A slice of the periodic  $800^3$  overlapping spherical particle microstructure, used as a “real” material to illustrate the new method described in this paper. Phase 0 is light gray, phase 1 is mid-gray, and phase 2 is dark gray.

We can also understand these volume fractions analytically, which will be a measure of the faithfulness of the digital representation. In a two phase infinite system of matrix plus identical overlapping objects, randomly centered, the remaining matrix volume fraction is given by (Xia and Thorpe, 1988; Mark, 1954):

$$c_0 = \exp(-nV) \quad (9)$$

where  $V$  = the volume of one object and  $n$  = the number of objects per unit volume. For any finite realization of this kind of microstructure, even if continuum rather than digital objects are used, eq. (9) will be an estimate only. In the case considered here,  $V$  = volume in voxels of a 41 voxel diameter sphere = 36137. The true volume of a 41 unit diameter sphere is 36086.95. In the system considered,  $n = 14\,850/(800^3) = 1.0481142$ . Therefore, the matrix volume fraction is predicted to be 0.3505983, which differs by only about 1 part in 700 from the theoretical value, probably due mainly to the small digital error in using digitized spheres vs. continuum spheres (Garboczi et al., 1991) and the fact that we have a finite realization. The inclusion volume fraction is predicted to be 0.6464017, which is very close to the sum of the volume fractions of phases 1 and 2. Note that the phase 1 and 2 volume fractions are simply predicted to be  $0.6464017 \cdot 0.3 = 0.1939205$  and  $0.6464017 \cdot 0.7 = 0.4524812$ , which are again very close to what is actually found digitally.

Two choices of elastic moduli were assigned to the three phases, as given in Table 2. This was done since it is known that the effect of local microstructure is enhanced with higher elastic moduli contrast between phases (Douglas and Garboczi, 1995; Garboczi et al. 2006; Garboczi

and Douglas, 2012), so that this choice could affect the elastic results with different boundary conditions. In a two phase composite, if the elastic moduli of each phase were the same, then the entire composite would have the same moduli. As the moduli of one phase begins to differ from the other, there are exact expansions in powers of these differences (Torquato, 2002) where the lower order terms, quadratic and below, do not depend at all on microstructure, while the higher order terms, past quadratic, which become more important with increasing phase elastic moduli contrast, do depend sensitively on microstructure.

Table 2: The phase elastic moduli for the two cases considered.

	$E_0$	$\nu_0$	$E_1$	$\nu_1$	$E_2$	$\nu_2$
Case 1	10 GPa	0.3	30 GPa	0.2	20 GPa	0.2
Case 2	10 GPa	0.3	150 GPa	0.2	60 GPa	0.2

A cylindrical piece, of diameter 760 voxels and height 800 voxels, is taken from the original  $800^3$  microstructure to simulate either a piece cored out of a real material and scanned on an X-ray CT or else a virtual core measured by internal scanning on some X-ray CT instruments. In any case, it serves as our “experimental” sample. Figure 3 shows a slice from the composite system with uniform medium (black) around the cylindrical core.

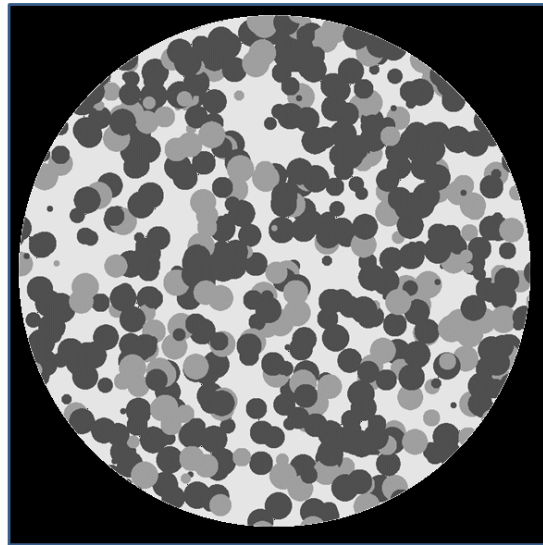


Figure 3: A 760 voxel diameter piece of the full cross-section, shown in Fig. 2, of the cylindrical simulated X-ray CT image, embedded in a uniform medium. In the microstructure, phase 0 is light gray, phase 1 is mid-gray, phase 2 is dark gray, and phase 3, the uniform medium surrounding the slice, is black.

For our sub-sampling, we choose cubes of two sizes, 100 voxels and 200 voxels on a side. The cube sampling is taken from the cylindrical core shown in Fig. 3. The best way to take a maximum number of non-overlapping cubic sub-samples from the 760 voxel diameter cylindrical core is illustrated in Fig. 4 for the  $100^3$  sub-samples, and in Fig. 5 for the  $200^3$  sub-samples.

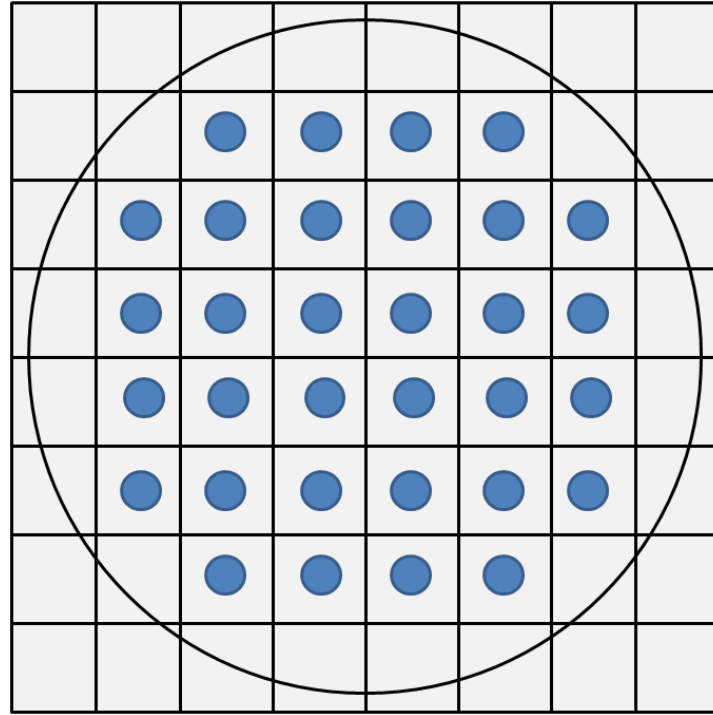


Figure 4: A schematic illustration of how the  $100^3$  voxel cubic sub-samples are taken from the cylindrical X-ray CT sample. 32 of 64 possible  $100^2$  pieces are taken out of each circular slice—solid color disks mark the squares that can be used. Eight contiguous 100 voxel thick slices are taken in the vertical direction, for a total of  $32 \times 8 = 256$   $100^3$  voxel cubic sub-samples.

Figure 4 shows how thirty-two non-overlapping  $100 \times 100$  squares can be taken from inside the circular cross-section of the cylindrical core. Since the core is 800 voxels high, eight non-overlapping layers of 100 voxel high cubes can be taken for a total of  $256$   $100^3$  non-overlapping cubic sub-samples that can be taken from within the cylindrical core. Figure 5 illustrates how seven  $200 \times 200$  non-overlapping squares can be optimally fit inside the circular cross-section of the cylindrical core. Since the core is 800 voxels high, four layers of non-overlapping 200 voxel cubes can be taken for a total of  $28$  non-overlapping  $200^3$  cubic sub-samples that can be taken from within the cylindrical core.

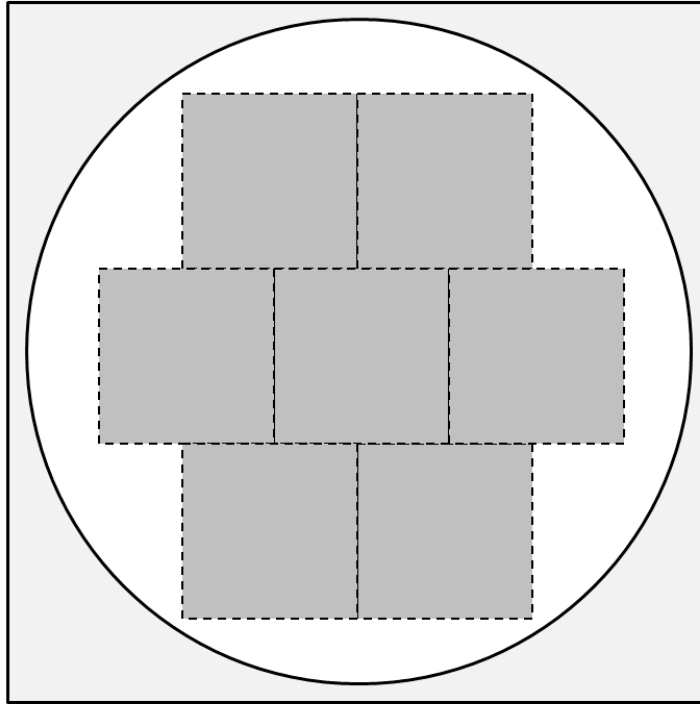


Figure 5: A schematic illustration of how the  $200^3$  voxel pieces are optimally taken from the circular cylinder part of the microstructure. Seven of 16 possible  $200^2$  pieces (dark gray) are taken out of each circular slice, and four 200 voxel-thick slices are taken in the vertical direction, for a total of  $7 \times 4 = 28$   $200^3$  cubes. The 760 voxel diameter circle is shown (white) and the full  $800^2$  slice (light gray).

The first parameter to consider when evaluating how well an average over sub-samples compares to the entire structure is the average and standard deviation of the three phase fractions taken over all the sub-samples of each size. The top part of Table 3 shows the results obtained for each kind of sub-sample and the actual deviation from the full  $800^3$  sample, whose phase volume fractions are considered to be the correct values. The “Volume fraction sampled” column adds up the volumes of each type of microstructure sub-sample used and lists the fraction of the total volume this represents. In the bottom portion of Table 3, the average for the two different size cubic sub-samples are taken over the entire  $800^3$  original system, so that the average phase fractions are the same as the complete structure, but with a non-zero standard deviation. Essentially, we are computing the phase fractions based on different size “windows” [Lu and Torquato, 1990; Quintanilla and Torquato, 1997]. These references demonstrate that the computed standard deviation in phase fraction decreases as the size of the window increases. In all cases, this value is much larger than the actual deviation of the average from the nominal  $800^3$  system value. Note that the standard deviations computed over only the cubes falling inside the

Table 3: Average phase fractions averaged over various size and shape microstructure sub-samples. The  $\Delta$  values are defined as: sub-sample value – full  $800^3$  system value.

System	Volume fraction sampled (%)	$c_0$	$\Delta_0$	$c_1$	$\Delta_1$	$c_2$	$\Delta_2$
$800^3$ periodic	100	0.3501	0	0.1962	0	0.4538	0
X-ray CT cylinder	70.9	0.3521	0.002	0.1925	-0.0037	0.4554	0.0016
Cube-100	50	0.3523	0.0022	0.1978	0.0016	0.4499	-0.0039
Cube-200	43.75	0.3507	0.0006	0.2000	-0.0038	0.4493	-0.0045
	# samples in average	$c_0$	$\sigma_0$	$c_1$	$\sigma_1$	$c_2$	$\sigma_2$
Cube-100	512	0.3501	0.0636	0.1962	0.0578	0.4538	0.0704
Cube-200	64	0.3501	0.0219	0.1962	0.0223	0.4538	0.0268

cylindrical sample, as shown in Figs. 3 and 4, are very close to the values listed in Table 3 and so are not listed. On comparing the Cube-200 result for  $c_0$  and the equivalent Cylinder-760 result, even though they are numerically very close in value, one must remember that the much larger standard deviation in  $c_0$  for the Cube-200 (listed in the bottom of Table 3) would mean that the actual value of  $c_0$  for a single sub-sample chosen has a much greater chance of being inaccurate than a single Cylinder-760 specimen.

As was mentioned earlier, when sub-sampling a microstructure scanned by X-ray CT for finite element computations, the usual practice is to clip out a cubic piece of microstructure. The boundary conditions usually involve fixed stress or fixed displacement or some combination of both. Another choice, which is rarely used, is to force periodic displacement boundary conditions, even though the microstructure is not periodic. In both cases, imposing various strain combinations enables the entire elastic moduli tensor of the sample to be computed. We wish to compute the elastic moduli of our two sets of cubic sub-samples,  $100^3$  voxels and  $200^3$  voxels. We used forced periodic boundary conditions, with enough strains to determine the elastic moduli tensor as detailed in Section 2, and also imposed fixed displacement boundary conditions to do the same. In this case, the outer nodes of the voxels were given an initial displacement, consistent with the applied strain, and then fixed throughout subsequent relaxation – a conjugate gradient solver routine is used to solve for the stored energy minimum.

Table 4 shows the results for the elastic moduli averages and computed standard deviations. The first row of Table 4 shows the computed Case 1 elastic moduli for the original  $800^3$  original system using periodic boundary conditions on this geometrically periodic structure. We take these as the “correct” or “bulk” material properties. The next row, marked “Cylinder-760-800”,

gives the elastic moduli computed using the new method for the cylindrical simulated X-ray CT sample that has been cut out of the original structure and surrounded by an uniform matrix. These computed moduli are the best possible for this sample, since all of the microstructure has been equally accessed using our new method. The agreement with the original material property is quite close, 0.2 % to 0.3 %. This tells us that the sample size was large enough to adequately capture the microstructure of the true material.

The next four rows of Table 4 give the elastic moduli for the  $100^3$  and  $200^3$  sub-samples averaged over all sub-samples. The standard deviation for each set is given, and two kinds of boundary conditions were used, forced periodic and fixed displacement. For both size sub-samples, the average elastic moduli for the forced periodic boundary conditions are significantly closer to the true material properties than are the averages using the fixed displacement properties. The fixed displacement boundary condition results are always significantly higher than the periodic boundary condition results, since adding constraints usually leads to higher elastic energies, so that the boundary nodes cannot freely move to minimize the stored elastic energy. The standard deviations in the elastic moduli for a given sub-sample size are similar for either boundary condition. The larger sub-sample results have smaller standard deviations, demonstrating that the standard deviations depend mainly on sample size (window) and not the choice of boundary conditions. The  $200^3$  forced periodic boundary average moduli agree as well with the true elastic moduli as do the cylinder results. However, since the standard deviation for K is about 1.6 % and for G about 2.6 %, this would imply that any single sub-sample would give elastic moduli that varied, on average, by this amount from the true values.

The lower portion of Table 4 lists the same results but for elastic moduli Case 2, where there is a greater contrast between the elastic moduli of the three phases. The true elastic moduli for the original random system more than double. We find that the error in the Cylinder-760-800 result to be about 1 % for both K and G. In the next rows, we find that the composite elastic moduli depend far more sensitively on the choice of sub-sample size and boundary condition due to the larger phase moduli contrast. Again, the results using the forced periodic boundary conditions do much better than the fixed displacement boundary conditions in agreeing with the full system results. The  $200^3$  voxel cubic sub-samples give average elastic moduli that agree with the full system moduli about as well as the cylinder results, but they have a much larger standard deviation than in Case 1, so that using only a few samples, as is usually done, would give an answer that is farther from the true result.

In Case 2 of Table 4, the average bulk and shear moduli from the  $100^3$  voxel cubes have significantly larger errors than in Case 1, for both types of boundary conditions. It is probably the case that a 100 voxel wide cube is not adequately capturing the local microstructure of the original random medium, since on average, only 2.5 41-voxel diameter spheres fit across a 100 voxel cube. This was also the situation in the Case 1 results, but was masked by the smaller contrast in phase elastic moduli. If all the phase moduli were the same, then microstructure does not matter at all. Also, if all phases had the same shear modulus but different bulk moduli, the

composite bulk and shear moduli would not depend at all on microstructure [Hill, 1963]. In Case 1, the two largest phases are 0 and 2, which both have the same shear moduli of 8.333, so this could also have helped to mask not adequately capturing the microstructure in the smaller cube samples.

Comparison between the compute time required for the  $100^3$ ,  $200^3$ , and full cylinder technique is interesting. We will focus on Case 2. The  $100^3$  sub-samples took a total of about 59 h using 50 processors, or 2 voxel layers per processor. The  $200^3$  sub-samples required 89 h using 100 processors, again 2 voxel layers per processor. The full cylinder computation used 194 h, employing 200 processors or 4 voxel layers per processor. If we had been able to use 400 processors, the compute time required would have been an estimated 100 h to 130 h, much nearer to the  $200^3$  computation.

One should note that for the system studied, the “real material”, the length scale of the microstructure was set by the 41 voxel diameter spheres used, so that a  $200^3$  cubic sub-sample was on the average 5 sphere diameters wide, which is often the rough rule of thumb used to tell if a unit cell is large enough, compared to the underlying microstructure, to achieve statistically valid results compare to the entire microstructure. So in this case, the  $200^3$  cubic sub-samples still contained enough of the microstructure to have a chance of achieving a statistically valid elastic moduli result. This was borne out by seeing in Table 4 that their average, using the forced periodic boundary conditions, was as close to the material properties as was the results for the new cylinder method. It is quite possible that the size of the cylindrical X-ray CT sample could be large enough to have a representative microstructure, but a smaller cubic sub-sample would not. This would be the case if larger spheres, say of 81-voxel diameter, had been used in the microstructure of the full system. In this scenario, the average over the  $200^3$  sub-samples would be much farther off from the true values and the results would have been similar to the  $100^3$  voxel cube samples presented earlier.

Table 4: Effect of boundary conditions on elastic moduli K, G obtained from cubic microstructure pieces compared to the true and simulated X-ray CT sample result.  $\Delta$  is the percent difference from the full system result.

System – Case 1	BC	Num	K (GPa)	$\Delta$ (%)	G (GPa)	$\Delta$ (%)
Original 800 <sup>3</sup> system	pd	1	10.8290		6.8811	
Cylinder-760-800	pd	1	10.8058	-0.2	6.8599	-0.3
Cube 100	pd	256	10.8437 $\pm$ 0.3776	0.14	6.9010 $\pm$ 0.4279	0.29
Cube 100	fixed disp	256	10.9097 $\pm$ 0.3849	0.75	7.1126 $\pm$ 0.4297	3.4
Cube 200	pd	28	10.8488 $\pm$ 0.1680	0.18	6.8970 $\pm$ 0.1765	0.23
Cube 200	fixed disp	28	10.8857 $\pm$ 0.1702	0.52	7.0259 $\pm$ 0.1785	2.1
System – Case 2	BC	Num	Micro. K	$\Delta$ (%)	Micro. G	$\Delta$ (%)
Full system	pd	1	22.9669		15.3006	
Cylinder-760-800-x	pd	1	22.7151	-1.1	15.1030	-1.29
Cube 100	pd	27	24.0076 $\pm$ 2.8601	4.53	16.2931 $\pm$ 2.4037	6.49
Cube 100	fixed disp	256	25.5132 $\pm$ 3.0783	11.1	18.5815 $\pm$ 2.5740	21.4
Cube 200	pd	27	23.1989 $\pm$ 1.1468	1.01	15.5403 $\pm$ 0.9624	1.57
Cube 200	fixed disp	28	24.4081 $\pm$ 1.2387	6.3	17.2418 $\pm$ 1.0331	12.7

## 6. Summary and conclusions

The main two problems with computing the effective elastic properties of pieces of real microstructure, which come from some kind of 3-D imaging system such as X-ray CT, is their large size, which leads to not being able to use all the microstructure information available, and applying appropriate boundary conditions so as to achieve a realistic result. We have used an existing parallel finite element method, where each voxel is a tri-linear finite element, which can handle these large sizes, up to or beyond 1000<sup>3</sup> voxel systems. By using a very large periodic model microstructure, whose elastic moduli were independently computed, we have essentially exact results against which to compare various sub-sampling and boundary conditions choices.

We have presented and validated a new method, where the cylindrical microstructure, as would be obtained in an X-ray CT experiment, is embedded in uniform material so that the entire structure can be simply treated with periodic boundary conditions. The effective elastic moduli of the cylindrical microstructure are then extracted from the composite result using highly accurate, analytical solutions of the simple composite geometry. If the cylindrical sample of the microstructure is all that is available, as in an X-ray CT image stack, then the entire

microstructure can be used and the resulting elastic moduli agree closely with the true result. For the specific case considered, where a  $200^3$  voxel sub-sample could contain a representative piece of the microstructure, the average of these cubic sub-samples agreed closely with the true result. However, the standard deviation was much larger than the deviation of the average from the true result, implying a loss of accuracy if only a few sub-samples were to be used. Finally, we have shown that if a cubic sub-sample needs to be taken from the entire microstructure image, forcing periodic displacement boundary conditions on a non-periodic sub-sample gives more accurate results than using fixed displacement conditions.

All programs used in this paper were in Fortran 90 and have been made available on-line. We note that this new method can also be used for electrical or thermal conductivity problems or thermoelastic problems in which exact solutions are available for sphere or cylinders in periodic square arrays.

## 7. Acknowledgements

We would to thank F. Sabina for preliminary discussions about the cylinder-box problem, A. Sangani for putting the two co-authors in touch with each other, C.L. Lin for useful conversations about this method and about aspects of X-ray CT, N. Kumar, D. Song, and C. Chan for suggesting looking at real microstructures taken from X-ray CT images, and USG and the NIST Sustainable Engineered Materials program for partial funding of this work.

## 8. References

C.L. Berman and L. Greengard, L., 1994. A renormalization method for the evaluation of lattice sums. *J. Math. Phys.* 35 6036-6048.

R.B. Bohn and E.J. Garboczi, 2003. User manual for finite element and finite difference programs: A parallel version of NIST IR 6269. NIST Internal Report 6997, U.S. Department of Commerce, Gaithersburg, Maryland.

J.F. Douglas and E.J. Garboczi, 1995. "Intrinsic viscosity and polarizability of particles having a wide range of shapes," *Advances in Chemical Physics* **91**, 85-153.

M. Faessel, C. Delisée, F. Bos, and P. Castéra, 2005. 3D Modelling of random cellulosic fibrous networks based on X-ray tomography and image analysis, *Composites Science and Technology*, Volume 65, 1931–1940.

E.J. Garboczi, M.F. Thorpe, M. DeVries, and A.R. Day, 1991. Universal conductivity curve for a plane containing random holes, *Physical Review A* 43, 6473-6482.

E.J. Garboczi and A.R. Day, 1995. An algorithm for computing the effective linear elastic properties of heterogeneous materials: 3-D results for composites with equal phase Poisson ratios. *J. Mech. Phys. of Solids* 43, 1349-1362.

E.J. Garboczi, 1997. <http://concrete.nist.gov/monograph>, button marked “Available software.”

E.J. Garboczi, 1998. Finite element and finite difference programs for computing the linear elastic and elastic properties of digital images of random materials. NIST Internal Report 6269, U.S. Department of Commerce, Gaithersburg, Maryland.

E.J. Garboczi, J.F. Douglas, and R.B. Bohn, 2006. A hybrid finite element-analytical method for determining the intrinsic elastic moduli of particles having moderately extended shapes and a wide range of elastic properties, *Mechanics of Materials* 38, 786-800.

E.J. Garboczi and J.F. Douglas, 2012. Elastic moduli of composites containing a low concentration of complex-shaped particles having a general property contrast with the matrix, *Mechanics of Materials* 51, 53-65.

E.J. Garboczi and V.I. Kushch, 2014. <ftp://ftp.nist.gov/pub/bfrl/garbocz/Code-for-CT-structures>. See README.pdf file in this directory.

G. Geandier, A. Hazotte, S. Denis, A. Mocellin, and E. Maire, 2003. Microstructural analysis of alumina chromium composites by X-ray tomography and 3-D finite element simulation of thermal stresses, *Scripta Materialia* 48,1219–1224.

Z. Hashin and S. Shtrikman, 1963. A variational approach to the theory of the elastic behavior of multiphase materials, *J. Mech. Phys. Solids* 11, 127-140.

R. Hill, Elastic properties of reinforced solids: some theoretical principles, 1963. *Journal of the Mechanics and Physics of Solids* 11, 357-372.

A.C. Kak and M. Slaney, 2001. *Principles of Computerized Tomographic Imaging*. SIAM, New York.

V.I. Kushch, 1987. Computation of the effective elastic moduli of a granular composite material of regular structure. *Soviet Appl. Mech.* 23, 362-365.

V.I. Kushch, S.V. Shmegeera, and L. Mishnaevsky, Jr., 2008. Meso cell model of fiber reinforced composite: interface stress statistics and debonding paths. *Int. J. Solids Struct.* 45, 2758-2784.

V.I. Kushch, S.G. Mogilevskaya, H.K. Stolarski, and S.L. Crouch, 2013. Elastic fields and effective moduli of particulate nanocomposites with the Gurtin-Murdoch model of interfaces. *International Journal of Solids and Structures* 50, 1141-1153

V.I. Kushch, 2013. *Micromechanics of composites: Multipole expansion approach*. Elsevier.

- S.A. Langer, E.R. Fuller Jr., and W.C. Carter, 2001. OOF: an image-based finite-element analysis of material microstructures, *Computing in Science and Engineering* 3, 15-23.
- B. Lu and S. Torquato, 1990. Photographic Granularity: Mathematical Formulation and Effect of Impenetrability of the Grains, *Journal of the Optical Society of America A* 7, 717-724.
- C. Mark, 1954. The expected number of clumps when convex laminae are placed at random and with random orientation on a plane area, *Proc. Cambridge Philos. Soc.* 50, 581-585.
- S. Meille and E.J. Garboczi, 2001. Linear elastic properties of 2-D and 3-D models of porous materials made from elongated objects, *Mod. Sim. Mater. Sci. and Eng.* 9, 371-390.
- G.W. Milton, 2002. *The Theory of Composites*. Cambridge University Press, Cambridge.
- A.B. Movchan, N.A. Nicorovici, and R.C. McPhedran, 1997. Green's tensors and lattice sums for elastostatics and elastodynamics. *Proc. R. Soc. Lond. A* 453, 643-662.
- T. Mura, 1982. *Mechanics of defects in solids*. Martinus Nijhoff, The Hague.
- W.T. Perrins, D.R. McKenzie, and R.C. McPhedran, 1979. Transport properties of regular arrays of cylinders, *Proc. R. Soc. Lond. A* 369, 207-225.
- B.E. Pobedrya, 1984. *Mechanics of Composite Materials*. Moscow State University Press.
- J. Quintanilla and S. Torquato, 1997. Local volume fraction fluctuations in random media, *Journal of Chemical Physics* 106, 2741-2751.
- Lord Rayleigh, 1892. On the influence of obstacles arranged in rectangular order on the properties of a medium. *Phil. Mag.* E 34, 481-502.
- A.P. Roberts and E.J. Garboczi, 2000. Elastic properties of model porous ceramics. *J. Amer. Ceram. Soc.* 83, 3041-3048.
- A.P. Roberts and E.J. Garboczi, 2002. Computation of the linear elastic properties of random porous materials with a wide variety of microstructure. *Proc. Roy. Soc. Lond. A* 458, 1033-1054.
- R. Rodriguez-Ramos, F.J. Sabina, R. Guinovart-Diaz, and J. Bravo-Castillero, 2001. Closed-form expressions for the effective coefficients of a fiber-reinforced composite with transversely isotropic constituents-I. Elastic and square symmetry. *Mech. Mat.* 33, 223-235.
- J.C. Russ, 2007. *The Image Processing Handbook*, CRC Press, Boca Raton.
- A.S. Sangani and W. Lu, 1987. Elastic coefficients of composites containing spherical inclusions in a periodic array. *J. Mech. Phys. Solids* 35, 1-21.
- G. Scocchi, A. Ortona, L. Grossi, G. Bianchi, C. D'Angelo, T. Leidi, and R. Gilardi, 2013. Evaluation of a simple finite element method for the calculation of effective electrical

conductivity of compression moulded polymer-graphite composites, *Composites Part A: Applied Sciences and Manufacturing* 48, 15-25.

S. Torquato, 2002. *Random Heterogeneous Materials: Microstructure and Macroscopic Properties*. Springer-Verlag, New York.

A. Tsuda, N. Filipovic, D. Haberthür, R. Dickie, Y. Matsui, M. Stampanoni, and J. C. Schittny, 2008. Finite element 3D reconstruction of the pulmonary acinus imaged by synchrotron X-ray tomography, *Journal of Applied Physiology* 105, 964-976. doi: 10.1152/jappphysiol.90546.2008

J.P. Watt and L. Peselnick, 1980. Clarification of the Hashin-Shtrikman bounds on the effective elastic moduli of polycrystals with hexagonal, trigonal, and tetragonal symmetries, *J. Appl. Phys.* **51**, 1525-1530.

J.P. Watt, 1980. Hashin-Shtrikman bounds on the effective elastic moduli of polycrystals with monoclinic symmetry, *J. Appl. Phys.* **51**, 1520-1524.

J.G.F. Wismans, J.A.W. van Dommelen, L.E. Govaert, and H.E.H. Meijer, 2010. X-ray computed tomography based modelling of polymeric foams, *Materials Science Forum* Vols. 638-642, 2761-2765. doi:10.4028/www.scientific.net/MSF.638-642.2761

W. Xia and M.F. Thorpe, 1988. Percolation properties of random ellipses, *Phys. Rev. A* 38, 2650–2656.

H. Yu, G. Cao, L. Burk, Y. Lee, J. Lu, P. Santago, O. Zhou, and G. Wang, 2009. Compressive sampling based interior reconstruction for dynamic carbon nanotube micro-CT, *J. X-Ray Science and Technology* 17, 295-303. DOI: 10.3233/XST-2009-0230.

## Appendix: Spherical microstructure sub-samples embedded in cubes

There are times when it may be useful to compute the effective elastic moduli of a spherical sub-sample of microstructure, or perhaps the entire sample is itself spherical, as could be the case of a particle of some kind. That way, the entire particle's moduli could be examined, not just a cubic piece, which could be important if the particle's skin had different elastic moduli than the particle's interior. If the overall shape of the microstructure is spherical, it can be embedded inside a cube and periodic boundary conditions used to compute the composite moduli in a manner similar to the cylinder method described in the main body of this paper.

Figure A1 shows a schematic illustration of this method applied to spheres. Note that using periodic boundary conditions means that the spherical sub-sample, of diameter  $D$ , does not have to be centered inside the cube. The edge length of the cube,  $L$ , should be selected to be at least 40 voxels larger than the diameter of the sphere, to allow for sufficient resolution of the length between sphere edges (also 40 voxels) to accurately solve for the stresses and strains in the embedding material. The sphere-cube system has cubic symmetry, so has three elastic moduli in general. The volume fraction of the sphere will be  $(D/L)^3$  times the maximum value,  $\pi/6$ .

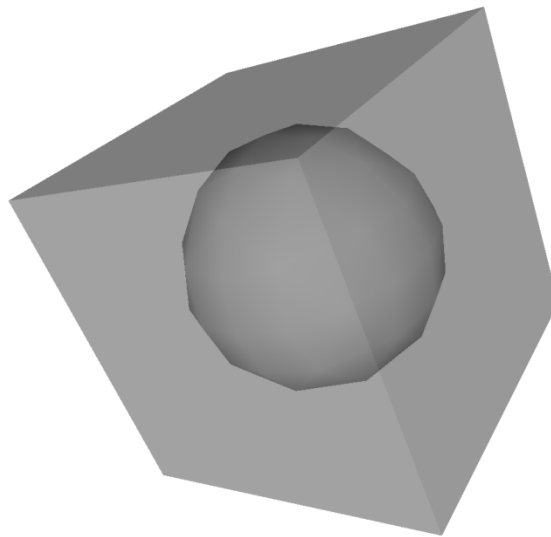


Figure A1: Schematic view of a spherical sub-sample centered inside a cubic unit cell.

The complete solutions of the homogenization problem for the linearly elastic composite containing a simple cubic array of identical spherical inclusions have been obtained independently in terms of Hasimoto's periodic potentials (Sangani and Lu, 1987) and in terms of vector solutions of the Lamé equation (Kushch, 1987). Despite some differences in technique and details, both solutions are based on the same, multipole expansion approach and are mathematically equivalent. A detailed account of the method is given elsewhere (Kushch et al., 2012; Kushch, 2013). Here, we show only the formulas used in our study.

The effective stiffness tensor of a periodic composite containing a simple cubic array of spherical

inclusions involves three independent components:  $C_{33}$  ( $= C_{11} = C_{22}$ ),  $C_{13}$  ( $= C_{23} = C_{12}$ ) and  $C_{44}$  ( $= C_{55} = C_{66}$ ). They are calculated in the same way as discussed in Section 3, by solving a series of unit cell problems and averaging the obtained local stress field. In fact, we need only two test cases to be considered: uniaxial applied strain  $\langle \varepsilon_j \rangle = \delta_{i3}$  and applied simple shear  $\langle \varepsilon_j \rangle = \delta_{i6}$ . The components  $C_{33}$  and  $C_{13}$  are found from the first test and  $C_{44}$  is found from the second one. These components are found from the following exact, finite form expressions:

$$\begin{aligned}\frac{2C_{13} + C_{33}}{3} &= K_0 + 3c(\lambda_0 + 2G_0)a_{00}^{(1)}, \\ C_{33} - C_{13} &= 2G_0[1 - 6c(1 - \nu_0)a_{20}^{(3)}], \\ C_{44} &= 2G_0[1 - 6c(1 - \nu_0)Re a_{21}^{(3)}]\end{aligned}$$

The vector dipole moments  $a_{00}^{(1)}$ ,  $a_{20}^{(3)}$  and  $a_{21}^{(3)}$  entering these expressions are uniquely determined from a system of linear algebraic equations analogous to eqs. (4) and (6). For the explicit form of the linear system and Fortran 90 source code for the evaluation of  $C_{ij}$ , see (Kushch, 2013).

A spherical test case has  $D = 200$  and  $L = 240$ , with  $E_0 = 1$ ,  $\nu_0 = 0.4$ ,  $E_1 = 10$ , and  $\nu_1 = -0.5$ . The volume fraction of the sphere in the 3-D digital system is 0.30301620, and the composite elastic moduli calculated were  $K = 5/3$  and  $G = 0.72096501$ . Note that both phases 0 and 1 had  $K = 5/3$ . By examining the exact Hashin-Strikman upper and lower bounds (Hashin and Strikman, 1963; Torquato, 2002) for a two-phase composite, when  $K_0 = K_1$ , the upper and lower bulk modulus bounds collapse to this common value forcing  $K = K_0 = K_1$ . Numerically, the composite result was also this same value to 8 or 9 significant figures. Table A1 shows the predictions for the composite sphere-box moduli, and then the predicted values of  $K_1$  and  $G_1$ , based on these composite moduli and the exact solution programs used in this paper. The percent error for both the forward calculation, between FEM and theory, is about the same as the inverse method error for  $K_1$  and  $G_1$ . As for the cylinder test case in Table A, the main reason for the difference between the theoretical and FEM predictions for the composite moduli is the voxel approximation to the curved spherical surface. Digital resolution scaling would improve this agreement substantially (Roberts and Garboczi, 2000, 2002; Garboczi et al. 2006; Garboczi and Douglas, 2012).

Table A1: The inverse problem for a sphere-box test case, where  $K_1$ ,  $G_1$  are the sphere moduli. The table lists the assigned values, the computed values, and the percent difference between them for  $K_1$  and  $G_1$ .

System (size in voxels)		Matrix (0)	Inclusion (1)	FEM composite	Theory composite	Diff (%)		Predicted inclusion modulus (1)	Diff (%)
Sphere (D=200) in cube (L=240)	Bulk modulus (GPa)	5/3	5/3	5/3	5/3	0		5/3	0
	Shear modulus (GPa)	5/14	10	0.720965	0.715399	0.8		10.125	1.25